Available online at www.sciencedirect.com
ScienceDirect
ELSEVIER
JOURNAL OF RARE EARTHS, Vol. 33, No. 2, Feb. 2015, P. 113
JOURNAL OF RARE EARTHS
www.re-journal.com/en/

Rietveld refinement and optical properties of $SrWO_4:Eu^{3+}$ powders prepared by the non-hydrolytic sol-gel method

P.F.S. Pereira[1], I.C. Nogueira[2], E. Longo[1], E.J. Nassar[3], I.L.V. Rosa[2], L.S. Cavalcante[4,*]

(1. Chemistry Institute, University of the State of Sao Paulo Julio de Mesquita Filho-UNESP, Francisco Degni, Araraquara-SP 14800-900, Brazil; 2. LIEC-Chemistry Department, Federal University of Sao Carlos, Via Washington Luis Km 235, Sao Carlos-SP 13565-905, Brazil; 3. University of Franca-UNIFRAN, Via Dr. Armando Sales de Oliveira, No. 201, Franca-SP 14404-600, Brazil; 4. CCN-DQ-GERATEC, University of the State of Piauí, Joao Cabral, 2231, P.O. Box 391, Terezina, PI 64002-150, Brazil)

Received 12 February 2014; revised 26 May 2014

Abstract: We investigated the effect of annealing time on the structure and optical properties of $SrWO_4:Eu^{3+}$ powders prepared by the non-hydrolytic sol-gel method and heat treated at 800 ºC for 2, 4, 8 and 16 h. Thermogravimetric and differential thermal analyses revealed that $SrWO_4:Eu^{3+}$ powders were obtained at about 800 ºC. X-ray diffraction patterns and Rietveld refinement data confirmed that all powders had a scheelite-type tetragonal structure. Micro-Raman and Fourier transform infrared spectra indicated structural order at short range and anti-symmetric stretching vibrations of O–W–O bonds associated with tetrahedral $[WO_4]$ clusters. Optical properties were investigated by ultraviolet-visible (UV-vis) diffuse reflectance, and photoluminescence (PL) data which provided the evolution of quantum efficiency (η) and lifetime (τ). UV-vis spectroscopy evidenced intermediate energy levels within the band gap of $SrWO_4:Eu^{3+}$ powders. PL properties validated that the Eu^{3+} electric-dipole ($^5D_0 \rightarrow {}^7F_2$) transition in PL emission spectra was dominant which proved that Eu^{3+} ions were positioned in a site without an inversion center. [($^5D_0 \rightarrow {}^7F_2$)/($^5D_0 \rightarrow {}^7F_1$)] band ratios showed that Eu^{3+} ions were located in a low symmetry environment. The PL emission, η and τ proved the dependence on the annealing time in the behavior of $SrWO_4:Eu^{3+}$ powders with a higher relative emission PL intensity as well as higher η and τ values related to other samples when heat treated at 800 ºC for 8 h.

Keywords: $SrWO_4$; Rietveld refinement; optical band gap; Eu^{3+}-rare earth; luminescence

Luminescent materials are known to exhibit a wide variety of applications such as solid state lasers, cathode ray tubes, phosphors for televisions, fluorescent tubes, medical images (X-rays, tomography) and devices in the production of artificial light[1,2]. White-light-emitting diodes (WLEDs) appear as light sources in the solid state with economic advantages in energy and maintenance as well as positive effects on the environment; WLEDs can replace traditional light sources such as incandescent and fluorescent lamps. Therefore, several research advances have been realized in light emission diodes (LEDs) which consist of a merger with the light blue or radiation near to the ultraviolet (UV) to obtain white light. When excited at 254 nm, conventional phosphors have a dominant emission band from the mercury lamp which is used for this purpose[3]. In phosphor converters of white light, the wavelength of excitation is higher at around 380 to 480 nm where the LED light emissions occur. New materials are being developed with high efficiency which can be efficiently excited at these wavelengths[3]. The luminescence efficiency of phosphors such as $Y_2O_2S:Eu^{3+}$, $BaMgAl_{10}O_{17}:Eu^{3+}$, $CaS:Eu^{3+}$, $SrY_2S_4:Eu^{3+}$ [4–7], used in color TVs is very low near UV irradiation. These phosphors are deficient in red emission, so consequently there has been growing interest in the discovery and development of new materials which emit white light with high UV absorption to emit in the red region[4-7]. Moreover, new compounds formed by the combination of tetrahedral [MoO_4, WO_4, PO_4 and VO_4] clusters are excellent host matrices for phosphors due to their excellent chemical and thermal stability[3,6–8]. The stability of a host matrix is active depending upon the geometry where each metal atom is coordinated to oxygen atoms and tetrahedral distortions[9–11]. Trivalent lanthanide ions (RE^{3+}) doped in tungstates are widely known as functional materials having unique physical and chemical properties[12]. Physical properties of these materials are strongly dependent on lattice defects formed when they are doped by other ions. The difference in electronic density between the dopant and host cations as well as the differences in electronic structures has proven to be the most important factor which involves the production of lumi-

Foundation item: Project supported by Brazilian Research Financing Institutions: Conselho Nacional para o Desenvolvimento de Pesquisa (CNPq) (142760/2008-0; 479644-2012-8; Postdoctoral 160922/2012-7), Fundação para o Amparo a Pesquisa do Estado de São Paulo (FAPESP), and Conselho de Aperfeiçoamento de Pessoal de Nivel Superior (CAPES)

* **Corresponding author:** L.S. Cavalcante (**E-mail:** laeciosc@bol.com.br; **Tel.:** +55 86 3213 7281)

DOI: 10.1016/S1002-0721(14)60391-4

nescent centers[13–15]. Therefore, the incorporation of trivalent dopants within different scheelite-type structures has been studied[13].

Tungstates and molybdates possess structural formulas of ABO_4, where A=Ca, Sr, Ba, Pb, Cd and B=W, Mo. These compounds crystallize in the ($I4_1/a$) space group and point symmetry equivalent to C_{4h}^6 [16–18]. Lattice parameters and unit cell volumes were evaluated as $a=b=$ 0.54168 nm, c=1.1951 nm and V=0.35066 nm^3, respectively, with four molecules in each crystallographic cell (Z=4) at room temperature[19]. In this type of structure, A^{2+} ions are surrounded by eight adjacent tetrahedral WO_4^{2-} [16–18] in a dodecahedral cluster approximation in the point group symmetry (C_{4h}^6) which is related to the site symmetry (S_4); B^{6+} ions are surrounded by four equivalent oxygen sites which form a tetragonal structure[13,20]. Trivalent rare-earths (RE^{3+}) provides a favorable situation for the substitution of A-sites with a perfect isostructural exchange[13,15]. Due to differences in valence states and sizes of W^{6+} (0.042 nm) and Eu^{3+} (0.107 nm) ions, the Eu^{3+} ion is expected to occupy only Sr^{2+} (0.113 nm) sites[21]. This occupancy is possible since electronic densities and coordination numbers of Eu^{3+} and Sr^{2+} ions are very similar[2,13,14,22–24]. Recently molybdates and tungstates doped with Eu^{3+} of the scheelite structure have been developed as red phosphors[5] for white LEDs. These materials have a strong charge transfer band (CTB) in the UV region[4–8] and an intense excitation of the Eu^{3+} ion at around 393 and 464 nm[25]. Under excitation at the UV range, the energy is transferred to the activator ion by non-radiative mechanisms[2,9]. This Eu^{3+} ion intensity is obviously enhanced in these matrices as compared with other matrices doped with the same ion[5]. When inorganic materials are doped with a certain amount of Eu^{3+} ions, the resulting product can be used as a potential phosphor for white light by combining blue-green light with the CTB of the O→W in tungstate materials and the red light characteristic of Eu^{3+} ions[12]. RE^{3+} doped inorganic matrices represent a family of materials with significant technological importance based on electronic, optical and chemical characteristics due to 4*f*-orbitals protection[24,26]. Most of their electronic properties are derived from the size, shape, crystal types and compositions which depend on synthesis processes[2,12,27]. Different methods have been employed in the synthesis of inorganic materials such as molten salts[12], microwave[18], Czochralski[28], Pechini[29], co-precipitation[28,30], galvanic cells[29], electrochemical cells[29], precursor polymeric[28], solid state reactions[28–30] and sol-gel[31]. Among these methods, the sol-gel process has advantages, including easy stoichiometric control, good homogeneity and low calcination temperatures. In general, prepared samples possess small sizes and narrow particle size distributions that promote good luminescent properties.

Therefore, the main objective for this paper was to synthesize strontium tungstate ($SrWO_4$) powders doped with Eu^{3+} ions by the non-hydrolytic sol-gel (NHSG) method and heat treated at 800 ºC for 2, 4, 8 and 16 h, respectively. Crystallization processes for precursors were evaluated by thermogravimetric (TG) and differential thermal analyses (DTA). The structure was confirmed by X-ray diffraction (XRD), Rietveld refinement data, micro-Raman (MR) and Fourier transform infrared (FT-IR) spectroscopies. Moreover, their optical properties were investigated by UV-vis diffuse reflectance spectroscopy and PL measurements at around 25 ºC and at 77 K.

1 Experimental

1.1 NHSG synthesis of $SrWO_4$ powders doped with Eu^{3+} ions

$SrWO_4$ powders doped with 1.0% of Eu^{3+} ions were synthesized as described in the previous study[31]. In this research, the powder was dried and pre-treated at 400 ºC for 4 h followed by heat treatment at 800 ºC for 2, 4, 8 and 16 h. In general, the chemical reactions involved between (Eu^{3+}/Sr^{2+}←WO_4^{2-}) ions resulted in crystalline $SrWO_4$:Eu^{3+} as shown in Eqs. (1) to (5):

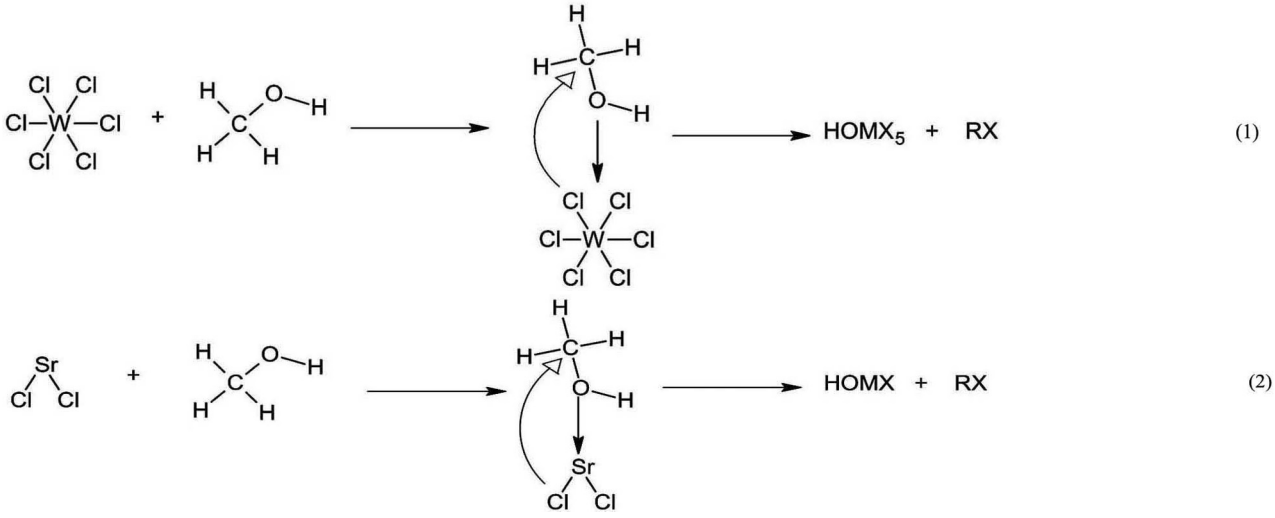

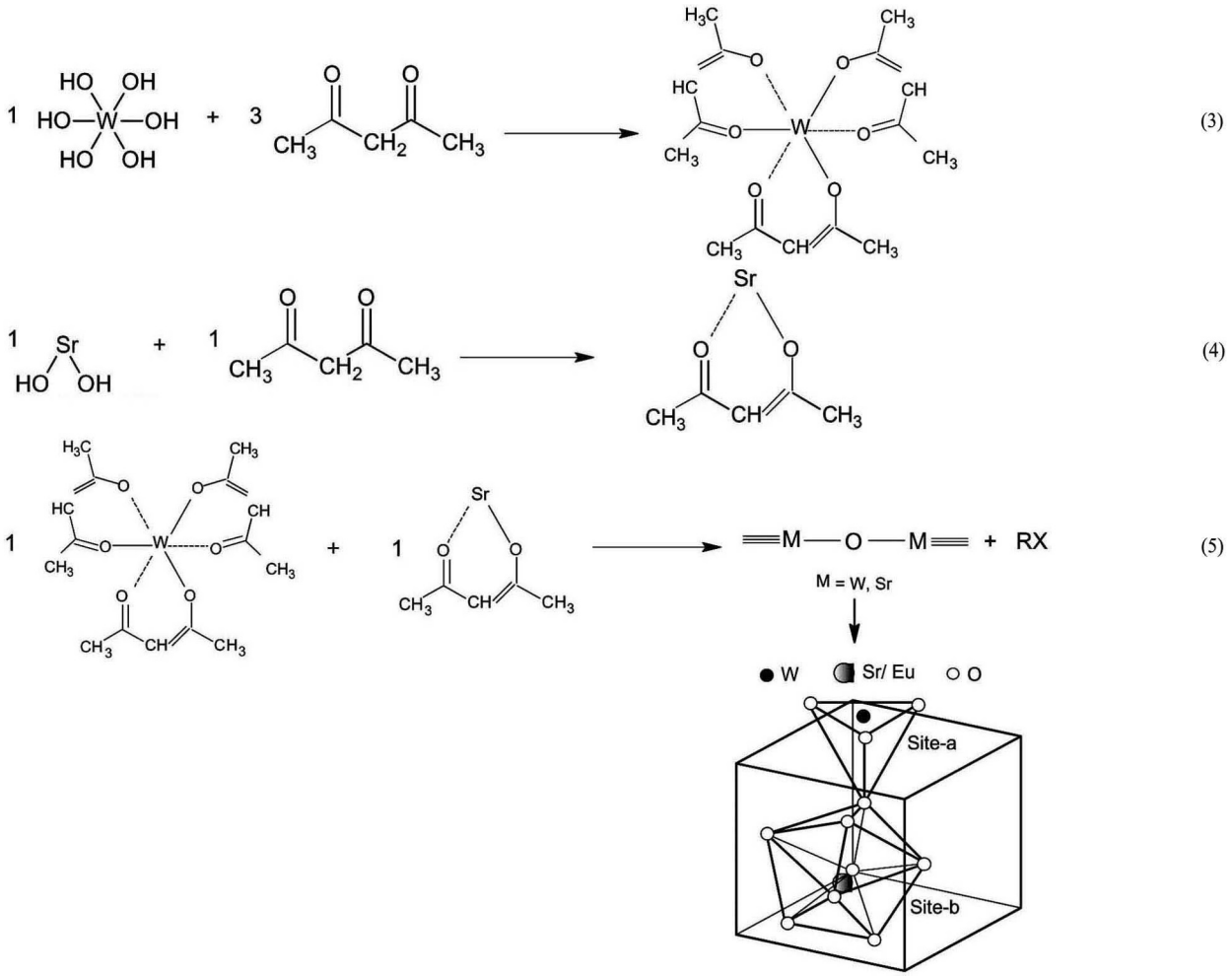

This oxide is formed by the condensation reaction of a metallic halide or semi-metallic (M–X) with an oxygen donor such as metallic alcoxide (M'–OR), ether (–ROR–) or alcohol (–OH–), under non-aqueous conditions to form inorganic oxide (M–OM')[32–34]. The reaction mechanism is shown in Eqs. (1–5) where the MeOH oxygen atom (Lewis base) coordinates with the center of the metallic halide WCl_6 or $SrCl_2$ (Lewis acid) followed by the nucleophilic attack of the halogen on electrophilic atoms of carbon adjacent to the oxygen. The substitution of ligands can occur by bimolecular nucleophilic substitution, S_{N2} or unimolecular nucleophilic substitution, S_{N1}. The formation of the carbocation by the S_{N1} mechanism quickly rearranges into a more stable secondary carbocation and forms alkyl halide (R–X) as a by-product[35] as illustrated in Eqs. (1 and 2). Then the acetylacetone ($C_5H_8O_2$) in a 1:3 and 1:1 molar ratios related to the WCl_6 and $SrCl_2$, respectively, were mixed into these solutions which formed a complex to prevent precipitation (see Eqs. (3) and (4)). The reaction between W and Sr complexes in 1:1 molar ratios results in oxy-chlorides metallic formation with the release of alkyl halides (RX) (Eq. (5)). After pre-treatment at 400 ºC for 4 h, the organic group is eliminated, and the treatment is maintained at 800 ºC for different time to produce $SrWO_4$ oxide doped with Eu^{3+} with a scheelite structure composed of tetrahedral and deltahedral clusters (Eq. (5)).

1.2 Characterizations

A thermal analysis was carried out using Thermal Analyst 2100-TA Instruments SDT 2960 with simultaneous thermogravimetric (TG) and differential thermal analyses (DTA) under a synthetic air flow at a heating rate of 20 ºC/min, from 25 to 1000 ºC. Powders were structurally characterized by XRD using a Rigaku-DMax/2500PC equipment (Japan) with Cu Kα radiation (λ=0.15406 nm) in the 2θ range from 10º to 75º and a 2 (º/min) increment. Micro-Raman (M-Raman) spectra were recorded using a T-64000 Horiba Jobin-Yvon triple monochromator coupled to a CCD detector; results were obtained in the 50 to 800 cm^{-1} range. Infrared spectra were recorded using potassium bromide (KBr) pellets from Merck P.A in a Bomem-Michelson FT spectrophotometer, MB-102 model. UV-vis spectra were taken using a Varian spectrophotometer (Model Cary 5G, USA) in a diffuse reflectance mode. PL data were obtained under continuous Xe-lamp (450 W) excitation in a SPEX Triax 550 Fluorolog 3 spectrofluorometer at ~25 ºC and at liquid N_2 temperature. The detection was performed with a Peltier-cooled SPEX Synapse CCD. The emission was collected at 90º from the excitation beam, and the Eu^{3+} lifetime was evaluated through the decay curve set

of the excitation and emission wavelength at 393 and 614 nm, respectively.

2 Results and discussion

2.1 TG and DTA analyses

The investigation of crystallization processes and precursor decomposition was evaluated by TG and DTA. Fig. 1 shows typical TG and DTA curves for $SrWO_4:Eu^{3+}$ powders prepared by the NHSG method at room temperature.

The crystallization process for dry gel precursors could be divided into three stages according to the TG/DTA curves. The first stage has three distinct endothermic transformations with strong peaks at about 90 ºC (see DTA curve) which correspond to a mass loss of around 20% between 50 and 150 ºC as is shown on the TG curve. This mass loss originates from the volatilization of water molecules absorbed on the surface of the powder and the evaporation of alcohol. The second stage shows a mass loss of about 24% from 250 to 650 ºC with exothermic peaks at about 300, 420 and 490 ºC (see DTA curve) due to the pyrolysis of organic compounds. In this stage, the mass loss was assigned to the combustion of excess acetylacetone, a residual organic group of alcohol and the decomposition of chlorides such as alkyl halides or metal chlorides. In the third stage, the mass loss was about 3.0% at 800 ºC which can be ascribed to the disappearance of residual alkoxy groups in the mineral matrix. In addition, the sharp endothermic peak located at 807 ºC indicated the crystallization of the gel. Above these temperatures, the mass remained constant which indicates that combustion and decomposition processes of all organic material precursors were complete[5]. The crystallization of the $SrWO_4:Eu^{3+}$ powder is in accordance with the results of XRD patterns.

2.2 XRD pattern analyses

Fig. 2 shows a typical XRD pattern of $SrWO_4:Eu^{3+}$ powders prepared by the NHSG method heat treated at 800 °C for 2 h, 4 h, 8 h and 16 h.

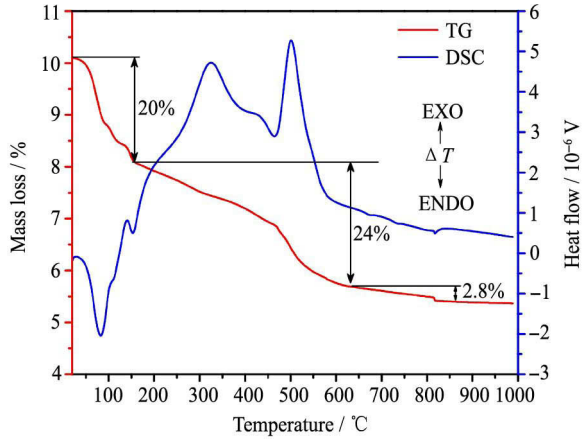

Fig. 1 TG and DTA curves for the precursors of $SrWO_4:Eu^{3+}$ powders prepared by NHSG method at room temperature

Fig. 2 shows a comparison of XRD patterns for samples with the ICSDS card No. 155425 which verifies that all XRD peaks are identified as pure $SrWO_4:Eu^{3+}$ powders; no extra peaks were detected, and almost all characteristic weak peaks were observed in XRD patterns. This result implies that the crystallinity and the degree of structural order at long range of $SrWO_4:Eu^{3+}$ powders are quite high and suggests an ordered structure[31] without any deleterious phases. Several peaks appear at 2θ=18.1º, 27.7º, 30.0º, 33.2º, 45.2º, 47.5º, 51.6º and 55.8º which can be, respectively, attributed to (101), (112), (004), (200), (204), (220), (116) and (312) reflections of the scheelite tetragonal structure of $SrWO_4:Eu^{3+}$ powders. All diffraction peaks can be indexed as a pure tetragonal structure with space group $I4_1/a$, cell parameters of a=b=0.5416 nm and c=1.1951 nm and a unit cell volume of 0.35056 nm^3 which are in agreement with the respective ICSDS card No. 155425[16,20,36]. In addition, XRD patterns revealed the absence of diffraction peaks attributed to the europium oxide (Eu_2O_3) which suggests that $SrWO_4:Eu^{3+}$ powders were obtained in their pure species.

Average crystallite sizes were estimated by the Scherrer's equation using the full width at half maximum (FWHM) of the most intense peak (112). The Scherrer's equation was explained in the previous study[31]. Based on this equation, average crystallite sizes of four samples of $SrWO_4:Eu^{3+}$ powders annealed at 800 ºC for 2, 4, 8 and 16 h were estimated at 58, 61, 66 and 62 nm. An increase in the annealing time facilitates an improvement in the intensity of XRD peaks for $SrWO_4:Eu^{3+}$ powders.

2.3 Rietveld refinement data analyses

Figs. 3(a–d) illustrate Rietveld refinement plots of $SrWO_4:Eu^{3+}$ powders prepared by the NHSG method and heat treated at 800 °C for (a) 2 h, (b) 4 h, (c) 8 h, and (d) 16 h.

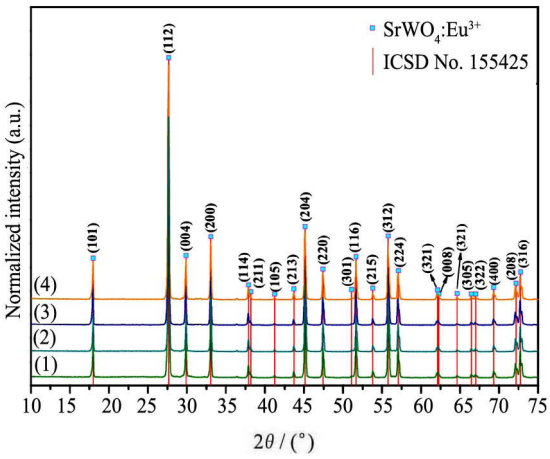

Fig. 2 XRD patterns of $SrWO_4:Eu^{3+}$ powders prepared by NHSG method heat-treated at 800 ºC for (1) 2 h, (2) 4 h, (3) 8 h, and (4) 16 h (The vertical lines indicate the Inorganic Crystal Structure Database (ICSD No. 155425))

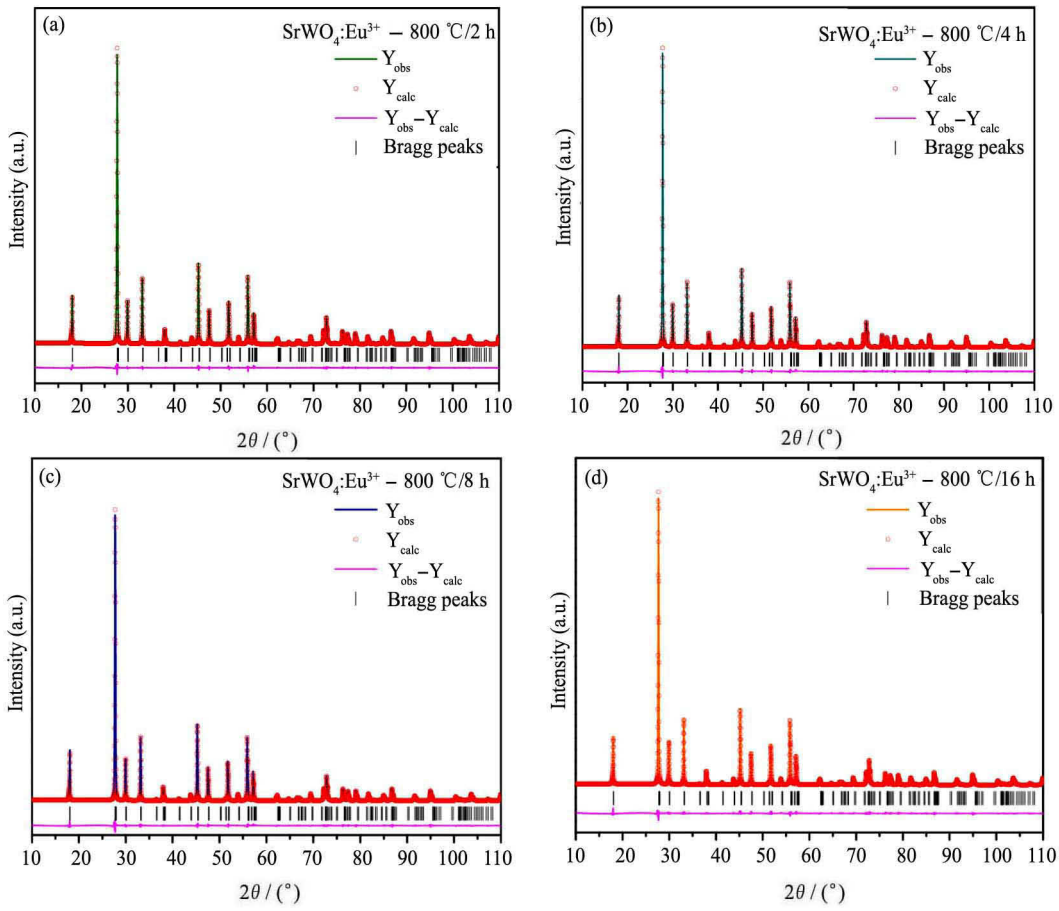

Fig. 3 Rietveld refinement plots of $SrWO_4:Eu^{3+}$ powders prepared by NHSG method heat-treated at 800 ºC for (a) 2 h; (b) 4 h; (c) 8 h; (d) 16 h

Rietveld refinement is a method where profile measurements of the intensity of the powder allow us to estimate an approximation of the structural model for the real structure. Figs. 3(a–d) show good agreement between observed XRD patterns and theoretical fit results which indicates the success of the Rietveld refinement method which is verified by small differences near to zero in the intensity scale as illustrated by a line (Y_{Obs}–Y_{Calc}) in Figs. 3(a–d). Values obtained through Rietveld refinement as well as (R_{wp}, R_{Bragg}, χ^2) coefficients, lattice parameters, volume cell and atomic coordinates of the unit cell are listed in Tables 1–3.

Table 1 indicates that the Rietveld refinement was performed with success and all the parameters listed above are acceptable for publication.

Table 2 lists lattice parameters and cell volume of $SrWO_4:Eu^{3+}$ powders obtained for different heat treatment time; no significant changes were observed. However, note that a small framework expansion occurs (in agreement with ICSDS card No. 155425), which causes a slight distortion in the environment. In comparison with samples at different heat treatment time, it can be verified that there is a reduction in the crystalline framework as confirmed by obtained lattice parameter (c) and cell volume values. It is believed that an effective competition exists between temperatures and treatment time variables which promotes the generation of structural defects in the $SrWO_4:Eu^{3+}$ lattice.

Table 3 shows atomic coordinates for O, Sr, Eu, and W atoms obtained by Rietveld refinement. According to these data, the environmental distortion is verified mainly from O atoms in (x, y, z) atomic coordinates

Table 1 Coefficients refinement of $SrWO_4:Eu^{3+}$ powders heat-teated at 800 ºC for 2, 4, 8 and 16 h

$SrWO_4:Eu^{3+}$ 800 ºC	R_{wp}/%	R_{Bragg}/%	χ^2
2 h	9.22	2.93	5.62
4 h	9.11	2.69	5.33
8 h	8.91	2.98	5.20
16 h	7.54	3.10	3.84

Table 2 Lattice parameters and volume cell of $SrWO_4:Eu^{3+}$ powders heat-treated at 800 ºC for 2, 4, 8 and 16 h

$SrWO_4:Eu^{3+}$ 800 ºC	Lattice parameters/nm		Volume/nm^3
	a=b	c	
2 h	$0.5418\pm2.5\times10^{-5}$	$1.1960\pm9.7\times10^{-5}$	$0.351099\pm4\times10^{-3}$
4 h	$0.5417\pm2.4\times10^{-5}$	$1.1959\pm9.6\times10^{-5}$	$0.350932\pm3\times10^{-3}$
8 h	$0.5417\pm2.2\times10^{-5}$	$1.1958\pm8.8\times10^{-5}$	$0.350918\pm4\times10^{-3}$
16 h	$0.5417\pm2.3\times10^{-5}$	$1.1959\pm9.1\times10^{-5}$	$0.350944\pm3\times10^{-3}$
ICSD	0.5416	1.1951	0.350559

Table 3 Atomic coordinates of the unit cell of $SrWO_4:Eu^{3+}$ powders heat-treated at 800 ºC for 2, 4, 8 and 16 h

Atoms	Site	$SrWO_4:Eu^{3+}$ (800 ºC/2 h)		
		x	*y*	*z*
O	16*f*	0.2374	0.1132	0.0444
Sr	4*b*	0	0.2500	0.6250
Eu	4*b*	0	0.2500	0.6250
W	4*a*	0	0.2500	0.1250
Atoms	Site	$SrWO_4:Eu^{3+}$ (800 ºC/4 h)		
		x	*y*	*z*
O	16*f*	0.2338	0.1129	0.0449
Sr	4*b*	0	0.2500	0.6250
Eu	4*b*	0	0.2500	0.6250
W	4*a*	0	0.2500	0.1250
Atoms	Site	$SrWO_4:Eu^{3+}$ (800 ºC/8 h)		
		x	*y*	*z*
O	16*f*	0.2325	0.1137	0.0454
Sr	4*b*	0	0.2500	0.6250
Eu	4*b*	0	0.2500	0.6250
W	4*a*	0	0.2500	0.1250
Atoms	Site	$SrWO_4:Eu^{3+}$ (800 ºC/16 h)		
		x	*y*	*z*
O	16*f*	0.2329	0.1100	0.0444
Sr	4*b*	0	0.2500	0.6250
Eu	4*b*	0	0.2500	0.6250
W	4*a*	0	0.2500	0.1250

while for Sr, Eu and W atoms, (*x*, *y*, *z*) atomic coordinates remain fixed in their characteristic positions. This phenomenon is based on the theory that Sr (4*b*), Eu (4*b*) and W (4*a*) atomic coordinates stay in special positions while for the O (16*f*), they are distributed in different positions in the crystalline lattice[37,38].

Tables 4 and 5 illustrate bond angle and bond length values for tetrahedral [WO_4] and deltahedral [SrO_8] clusters determined by modeling with the Diamond software (Crystal and Molecular Structure Visualization) version 3.2 g for Windows 7.

Small variations observed in $SrWO_4:Eu^{3+}$ powders (see Tables 4 and 5) obtained for different treatment time can be confirmed by angle and bond length values between tetrahedral [WO_4] and deltahedral [SrO_8] clusters.

2.4 Unit cell representation for $SrWO_4:Eu^{3+}$

Fig. 4 illustrates the unit cell representation for a $SrWO_4:Eu^{3+}$ tetragonal phase with space group ($I4_1/a$) which was modeled using Diamond software[39,40].

To model this unit cell, structural lattice parameters and atomic coordinates were used (see Tables 2 and 3). According to Fig. 4, Sr and Eu atoms are coordinated to the eight oxygen atoms which form deltahedral [SrO_8]/[EuO_8] clusters and disphenoid-type polyhedra (8 vertices, 12 faces and 18 edges)[11,18]. The W atoms are coordinated to four oxygen atoms which form tetrahedral [WO_4] clusters with a tetrahedral geometry slightly distorted[18,41] in accordance with data obtained with different bond angle values between oxygen atoms (see Tables 4 and 5). This simulation was conducted with $SrWO_4:Eu^{3+}$ powders heat treated at 800 °C for different treatment time (not illustrated), but only sample data treated for 8 h are shown in Fig. 4 where no significant changes between the unit cells were noticeable (only a slight distortion) (see Table 2).

2.5 M-Raman spectroscopy analyses

Fig. 5 shows M-Raman spectra from 50 to 800 cm^{-1} for $SrWO_4:Eu^{3+}$ powders prepared by the NHSG method and heat treated at 800 ºC for different time.

According to group theory[42], $SrWO_4:Eu^{3+}$ powders belong to point-group symmetry (C_{4h}^6) and space group ($I4_1/a$) at room temperature which contain two molecular formulas per primitive cell (Z=4). Based on the character of the point-group symmetry, optically active modes in Raman (R) and infrared (IR) spectra are represented in Eq. (6):

$$\Gamma_{vib}=3A_g\,(R)+5B_g\,(R)+5E_g\,(R)+4A_u\,(IR)+4E_u\,(IR) \quad (6)$$

In agreement with Eq. (6) regarding tungstates with a scheelite-type tetragonal structure, there are 26 different vibrational modes which are determined by calculations of group theory[43–45]. The first member pair "g" is a Raman-active mode, and the second member odd "u" is an infrared-active mode represented by the (*R*) and (*IR*), respectively. However, only $4A_u$ and $4E_u$ of $5A_u$ and $5E_u$ vibration modes are active in *IR* spectra, ($1A_u$ and $1E_u$) modes are acoustic vibrations and $3B_u$ are silent modes[43].

Table 4 Bond length to (W–O) and bond angle present into tetrahedral [WO_4] clusters

Tetrahedral [WO_4] clusters	Bond angle		Bond length/nm
	α/(º)	β/(º)	W–O
2 h	107.23	114.05	0.177
4 h	107.36	113.78	0.175
8 h	107.36	113.77	0.174
16 h	107.29	113.93	0.171

Table 5 Bond length to (Sr–O) and bond angle present into deltahedral [SrO_8] clusters

[SrO_8]	*α*/(º)	*β*/(º)	*γ*/(º)	*δ*/(º)	*ε*/(º)	*ζ*/(º)	*η*/(º)	*θ*/(º)	Bond length/nm Sr–O
2 h	68.1	73.6	76.7	78.1	97.8	127.9	136.7	149.3	0.258; 0.261
4 h	67.9	73.3	78.7	97.7	112.0	137.1	149.2	149.6	0.260; 0.262
8 h	67.8	73.1	77.2	79.1	97.6	127.6	137.4	149.0	0.261; 0.262
16 h	67.8	73.2	77.7	78.6	97.8	127.3	136.7	149.7	0.260; 0.261

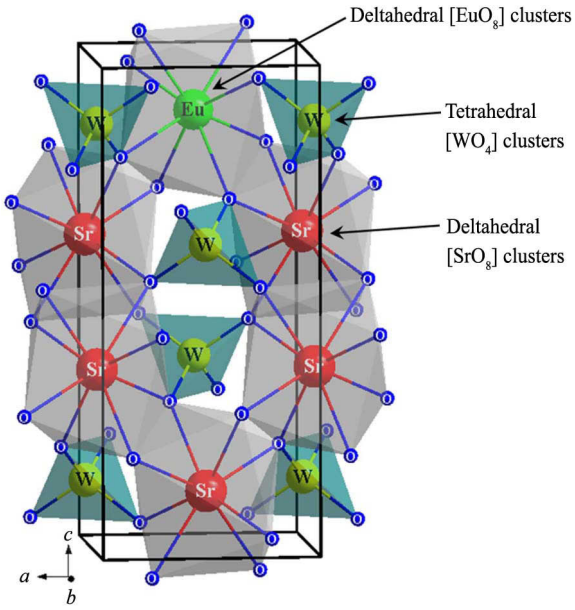

Fig. 4 Unit cell representation to $SrWO_4:Eu^{3+}$

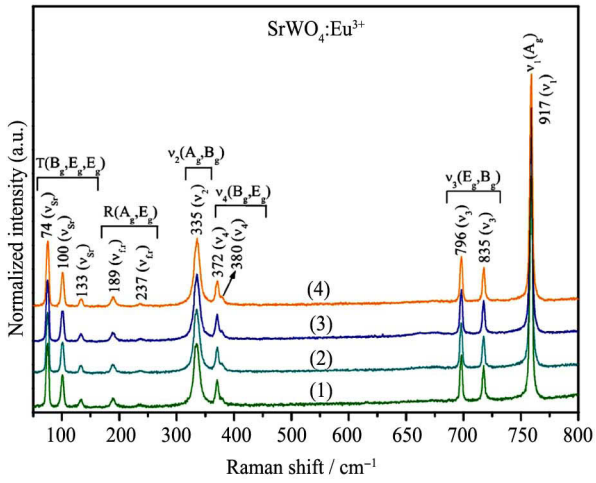

Fig. 5 M-Raman spectra of $SrWO_4:Eu^{3+}$ powders obtained by the NHSG method heat-treated at 800 ºC for (1) 2 h; (2) 4 h; (3) 8 h; (4) 16 h

Therefore, only 13 active modes are expected in Raman spectra, as represented by Eq. (6). These modes are classified as seven internal and six external modes, respectively, and correspond to four translations and two rotations which involve interactions with deltahedral [SrO_8] and tetrahedral [WO_4] clusters. Internal modes occur within unit molecular tetrahedral [WO_4] clusters where the center of mass remains stationary. External modes are lattice phonons and correspond to the motion of A^{2+} cations in rigid molecular units. Their vibrational modes are composed of [$\nu_1(A_1)$, $\nu_2(E)$, $\nu_3(F_2)$ and $\nu_4(F_2)$], one free rotation mode [$\nu_{f.r.}(F_1)$] and one translation mode (F_2)[43].

Fig. 5 confirms that all Raman peaks are strong and well defined. According to Basiev et al.[45], characteristically, these crystals have a covalent character in their bonds. Therefore, $SrWO_4:Eu^{3+}$ powders exhibit ionic bonds between cations and the molecular group in each crystal while covalent bonds dominate tetrahedral [WO_4] clusters[31]. In these crystals, the most intense modes correspond to internal vibrations within tetrahedral [WO_4] clusters.

Thus, by using Eq. (6), the existence of 13 vibrational modes in Raman spectra can be predicted. However, in this study, we observed only 11 Raman-active modes (see Fig. 5). The symmetric stretching and anti-symmetric stretching between O–W–O bonds at lower energies indicates a twist mode between O–W–O and O–Sr–O bonds. Therefore, Raman spectra show $3A_g$ vibrational modes (917; 335 and 189 cm^{-1}), $3B_g$ (835; 372; and 74 cm^{-1}) and $5E_g$ (796; 380; 237; 133 and 100 cm^{-1}). Two other Raman peaks which are not observed can overlap with other peaks. In agreement with results reported by Basiev et al.[46], an overlapping of ν_2 (A_g) by ν_2 (B_g) modes near 337 cm^{-1} occurs. The Raman peak at 917 cm^{-1} is attributed to the symmetric stretching ν_1 of O–W–O bonds while the peak at 335 cm^{-1} is assigned as ν_2 of the symmetric deformation which is related to symmetric bending O–W–O bonds. Peaks at 835 and 796 cm^{-1} are designated as ν_3 anti-symmetric modes which represent stretching of O–W–O bonds; peaks at 372 and 380 cm^{-1} are attributed to the ν_4 anti-symmetric deformation of O–W–O bonds[47]. Peaks located at 237, 189, 133, 100 and 74 cm^{-1} are designated as rotational (A_g, E_g) and translational (B_g) modes[48]. Free modes of tetrahedral [WO_4] clusters were observed at 237 and 189 cm^{-1}; peaks at 133, 100 and 74 cm^{-1} correspond to external modes of stretching and flexion actions of O–Sr–O bonds.

Moreover, the rise of processing time causes an increase in the structural organization at short range between the [WO_4]–[SrO_8]–[WO_4]–[EuO_8]–[WO_4] clusters. This behavior can be observed by the presence of Raman peaks more defined at 189 cm^{-1}, which is related to free rotation modes. Therefore, all Raman-active modes are well defined (see Fig. 5), which indicates that $SrWO_4:Eu^{3+}$ powders are all crystalline at short range.

2.6 FT-IR spectroscopy analyses

Fig. 6 shows IR spectra for $SrWO_4:Eu^{3+}$ powders synthesized by the NHSG method and heat-treated at 800 °C for 2, 4, 8 and 16 h.

The representation related to the tetrahedral symmetry is Γ_{Td} =[$\nu_1(A_1)$, $\nu_2(E)$, $\nu_3(F_2)$ and $\nu_4(F_2)$], but only $\nu_3(F_2)$ and $\nu_4(F_2)$ are infrared-active modes in FT-IR spectra[49]. Ling et al.[47] reported that E_u (826.6 cm^{-1}) and A_u (411.7 cm^{-1}) modes are optically active modes and are detected in FT-IR spectra. The absorption band in FT-IR spectra at 827 cm^{-1} is attributed to $F_2(\nu_3)$ of the anti-symmetric stretching of tetrahedral [WO_4] clusters while the band at 412 cm^{-1} is assigned to $F_2(\nu_4)$ with anti-symmetric deformation regarding O–W–O bonds. Bands at around 350 cm^{-1} can be assigned to ν_2 modes and are related to

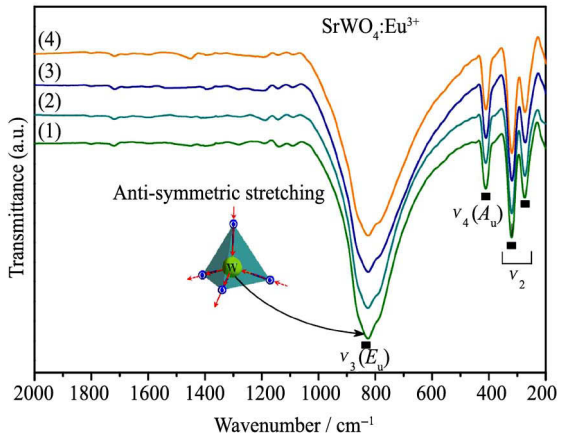

Fig. 6 FT-IR spectra of the $SrWO_4:Eu^{3+}$ powders in range from 2000 to 200 cm^{-1} heat-treated at 800 °C for (1) 2 h; (2) 4 h; (3) 8 h; (d) 16 h

the symmetric deformation in tetrahedral [WO_4] clusters which are located at 319 and 275 cm^{-1} due to distortions in deltahedral [SrO_8] clusters[47].

According to Nakamoto[50] the internal mode (v_2) which is related to symmetric deformation indicates an active vibration in Raman spectra, which is in agreement with the micro-Raman spectra (see Fig. 5). IR analyses revealed two internal modes (v_2) which are ascribed to the unique peak at 335 cm^{-1} in MR spectra. According to Basiev et al.[46] and group theory[42], a possible overlapping of $v_2(A_g)$ and $v_2(B_g)$ modes is visible near 337 cm^{-1}.

FT-IR spectra of two bands below 350 cm^{-1} indicate a phonon coupling energy between tetrahedral [WO_4] and deltahedral [SrO_8] clusters. According to the Ref. [47], IR-active vibrational modes at around 193 and 162 cm^{-1} correspond to stretching between O–Sr–O bonds in deltahedral [SrO_8] clusters. Moreover, infrared-active modes at 135 and 73 cm^{-1} were assigned to axial deformation in vibrations of O–W–O and O–Sr–O bonds, respectively. However, these regions were not detected by the equipment due to the spectral range from 200 to 4000 cm^{-1}.

FT-IR spectra show the same profile for all samples which indicates that heat treatment at different time did not modify stretching and deformation modes of O–W–O bonds. FT-IR spectra provided evidence that all $SrWO_4:Eu^{3+}$ powders have a scheelite-type tetragonal structure and do not show active modes relative to organic compounds remaining from the synthesis, which indicates the total decomposition of organic constituents when samples were heated at 800 °for different treatment time.

2.7 UV-vis absorption spectroscopy analyses

The optical band gap energy (E_{gap}) was calculated by the Kubelka and Munk method[51] which is based on the transformation of diffuse reflectance measurements to estimate E_{gap} values with good accuracy within the limits of assumptions[52]. This method is particularly useful in limited cases of an infinitely thick sample layer. The Kubelka-Munk equation for any wavelength is described by Eq. (7):

$$F(R_\infty)=\frac{(1-R_\infty)^2}{2R_\infty}=\frac{k}{s} \quad (7)$$

where $F(R_\infty)$ is the Kubelka–Munk function or absolute reflectance of the sample. In our case, magnesium oxide (MgO) was the standard sample in reflectance measurements. $R_\infty=R_{sample}/R_{MgO}$ (R_∞ is the reflectance when the sample is infinitely thick), k is the molar absorption coefficient, and s is the scattering coefficient. In a parabolic band structure, the optical band gap and absorption coefficient of oxide semiconductors[53] can be calculated by Eq. (8):

$$\alpha h\nu = C_1(h\nu - E_{gap})^n \quad (8)$$

where α is the linear absorption coefficient of the material, $h\nu$ is the photon energy, C_1 is a proportionality constant, E_{gap} is the optical band gap, and n is a constant associated with different kinds of electronic transitions (n= 0.5 for a direct allowed, n=2 for an indirect allowed, n= 1.5 for a direct forbidden and n=3 for an indirect forbidden). According to the literatures[54,55], tungstate materials exhibit an optical absorption spectrum governed by direct electronic transitions. In this phenomenon, after the electronic absorption process, the electrons located in maximum energy states in the valence band (VB) revert to minimum-energy states in the conduction band (CB) under the same point in the Brillouin zone[56]. Based on this information, E_{gap} values of $SrWO_4:Eu^{3+}$ powders were calculated using n=0.5 in Eq. (8). Finally, using the remission function described in Eq. (7) with $k=2\alpha$, the modified Kubelka-Munk equation was obtained as indicated in Eq. (9):

$$[F(R_\infty)h\nu]^2 = C_2(h\nu - E_{gap}) \quad (9)$$

Therefore, by finding the $F(R_\infty)$ value from Eq. (9) and plotting a graph of $[F(R_\infty)h\nu]^2$ against $h\nu$, we can determine E_{gap} values for our $SrWO_4:Eu^{3+}$ powders for different treatment time with greater accuracy by extrapolating the linear portion of UV-vis curves.

Figs. 7(a–d) show UV-vis spectra for $SrWO_4:Eu^{3+}$ powders synthesized by the NHSG method and heat-treated at 800 ºC for 2, 4, 8 and 16 h; their corresponding E_{gap} values obtained are listed in Table 6.

Figs. 7(a–d) show that an increase in heat treatment produces a decrease in E_{gap} values (see Table 6). According to Cavalcante et al.[57], this behavior indicates that there are structural defects in the $SrWO_4:Eu^{3+}$ powders and implies distinct organizations of intermediate states within the band gap. Thus, variations of E_{gap} energy are related to the degree of order-disorder of the lattice and the degree of distortion within tetrahedral [WO_4] clusters and deltahedral [SrO_8] clusters which are caused by the influence of temperature and treatment time (see

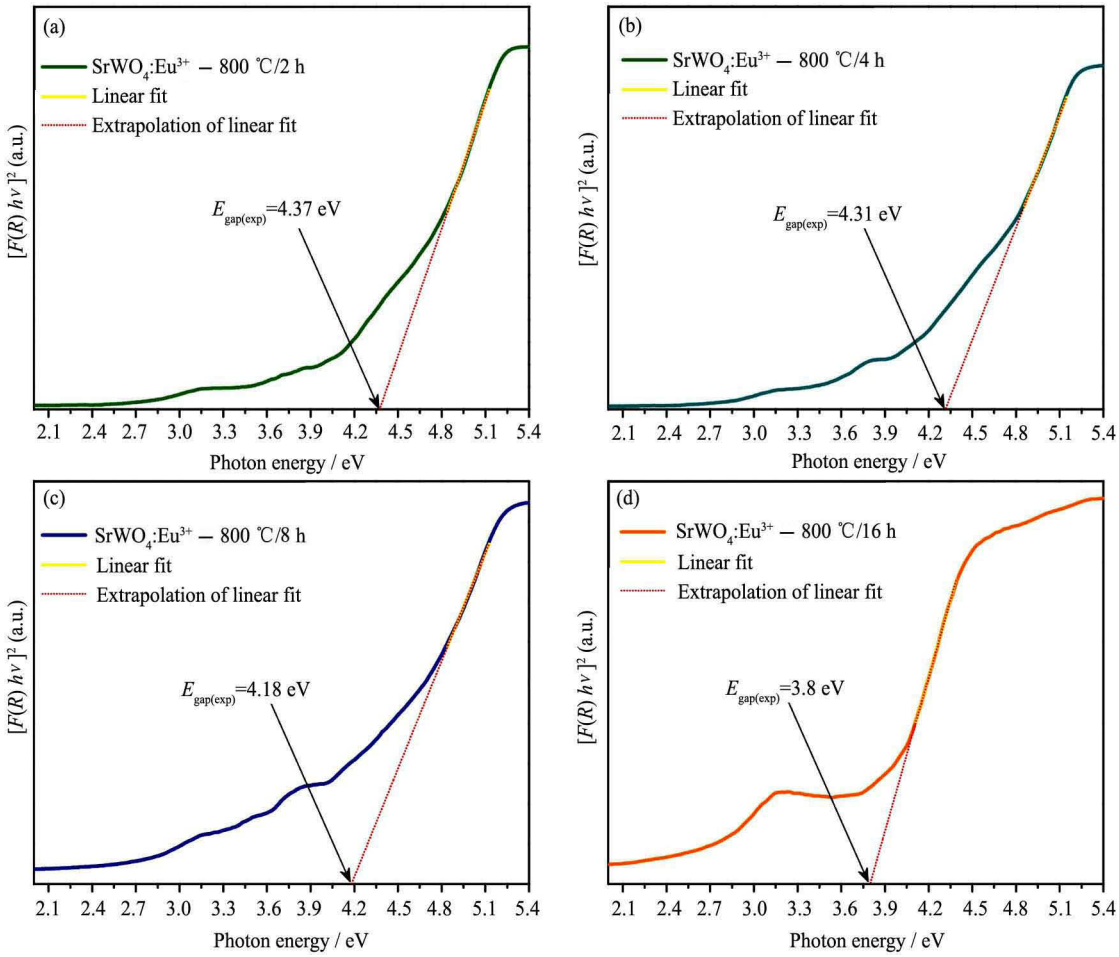

Fig. 7 UV-vis spectra for $SrWO_4:Eu^{3+}$ powders heat-treated at 800 °C for (a) 2 h; (b) 4 h; (c) 8 h; (d) 16 h

Figs. 7(a–d)). These relationships of order-disorder and/or structural distortions in Sr–O bonds and W–O bonds are due to the use of Eu^{3+} ions as dopants which promote distortions in (α, β) angles and in bond lengths which reflect directly on variations of lattice parameters and cell volumes (see Table 2). These various types of defects in the lattice promote different distributions in intermediate levels between the VB and CB[11,16,18,36,37,41]. Therefore, these modifications in the electronic structure affect optical properties of the material. Data obtained for the E_{gap} are corroborated with cell volume variations which decrease as the heat treatment time change.

Different types of structural defects can appear in $SrWO_4:Eu^{3+}$ crystals. These defects can also be attributed to oxygen vacancies caused by the introduction of Eu^{3+} ions into the lattice according to Eq. (10) below:

$$Eu_2O_3 \xrightarrow{SrWO_4} 2Eu_{Sr}^{\bullet}+V_{Sr}''+3O_O^x \quad (10)$$

The optical band gap behavior can be justified by the formation of strontium vacancies (V_{Sr}'') and complex oxygen vacancies which are able to show three different charge forms: neutral V_O^x, singly ionized $V_O^{\bullet}$ and double ionized $V_O^{\bullet\bullet}$. The V_O^x are able to donate up to two electrons, the $V_O^{\bullet}$ are donors or capture only one electron, and $V_O^{\bullet\bullet}$ are not able to donate electrons but can receive up to two electrons. These oxygen vacancies act as defects in the lattice of $(Sr_{1-x}Eu_{2x/3})WO_4$ crystals with x=0.01 and can be stabilized by charge compensation into the lattice. The necessity for charge compensation and the influence of temperature and treatment times causes a lattice distortion. According to the Ref. [58], oxygen vacancies induce new energy in the "band gap" and can be assigned to vacancies formed by tungsten-oxygen.

Table 6 E_{gap} values for the $SrWO_4:Eu^{3+}$ powders synthesized by NHSG method heat-treated at 800 ºC for different time

Samples	Shape	Temperature/ºC	Time/h	E_{gap}/eV
$SrWO_4:Eu^{3+}$	Powders	800	2	4.37
$SrWO_4:Eu^{3+}$	Powders	800	4	4.31
$SrWO_4:Eu^{3+}$	Powders	800	8	4.18
$SrWO_4:Eu^{3+}$	Powders	800	16	3.8

2.8 PL excitation and emission spectra analyses

Excitation spectra of $SrWO_4:Eu^{3+}$ powders synthesized by the NHSG method which are heat treated at 800 °C for 2, 4, 8 and 16 h monitored at 614 nm ($^5D_0 \rightarrow {}^7F_2$) are shown in Fig. 8(1–4).

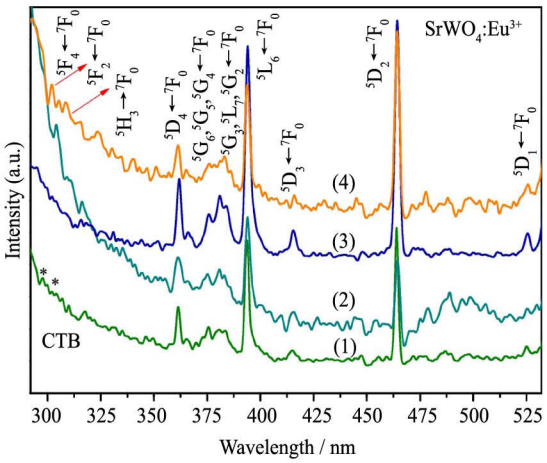

Fig. 8 PL excitation spectra of $SrWO_4:Eu^{3+}$ powders heat-treated at 800 °C
(1) 2 h; (2) 4 h; (3) 8 h; (4) 16 h

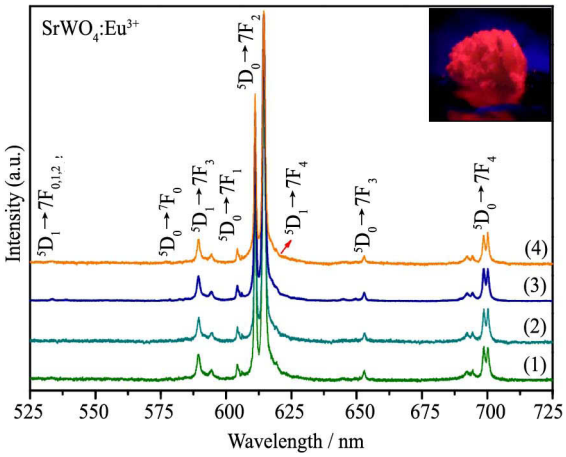

Fig. 9 PL emission of $SrWO_4:Eu^{3+}$ powders heat-treated at 800 ºC for 2 h (1), 4 h (2), 8 h (3), and 16 h (4), excited at 393 nm (Inset shows the picture of the powder emission at room temperature)

Fig. 8 illustrates that excitation PL spectra were performed in the range from 280 to 530 nm. An increase from 280 to 320 nm for all the spectra is notable and is attributed to charge transfer bands CTBs between the O→W and O→Eu[59]. In addition, these CTBs in the $SrWO_4:Eu^{3+}$ are attributed to electron transitions from the oxygen 2*p* orbital to the empty tungsten 5*d* orbital or to an empty Eu^{3+} 4*f* orbital[15,22]. This behavior is related to coupling between the lattice and luminescent centers. These couplings depend mainly on the distance from metal ions to ligands[15,22]. In the range from 295 to 550 nm, there are bands of *f-f* transitions that are characteristics of the intra-configurational of Eu^{3+} ions in all $SrWO_4:Eu^{3+}$ spectra. We identified and assigned the following transitions: $^5F_4\leftarrow{}^7F_0$ (298 nm), $^5F_2\leftarrow{}^7F_0$ (302 nm), $^5H_3\leftarrow{}^7F_0$ (317 nm), $^5D_4\leftarrow{}^7F_0$ (361 nm), $^5G_J\leftarrow{}^7F_0$ (*J*=2–6) in the range from 365 to 385 nm, $^5L_7\leftarrow{}^7F_0$ (381 nm), $^5L_6\leftarrow{}^7F_0$ (393 nm), $^5D_3\leftarrow{}^7F_0$ (416 nm), $^5D_2\leftarrow{}^7F_0$ (463 nm) and $^5D_1\leftarrow{}^7F_0$ (535 nm). The CTB with Eu^{3+} ion *f-f* transitions shows that an increase in the heat treatment time promotes a rise in the *f-f* transition intensities.

Fig. 8 illustrates that $SrWO_4:Eu^{3+}$ powders heat treated at 800 ºC for 2 and 16 h exhibit more intense $^5D_2\leftarrow{}^7F_0$ transitions in relation to $^5L_6\leftarrow{}^7F_0$ transitions. In $SrWO_4:Eu^{3+}$ powders heat treated at 800 ºC for 4 h, an inversion in the intensity of these transitions is visible; $^5L_6\leftarrow{}^7F_0$ transitions are preferred for this system. Powders heat treated at 800ºC for 8 h had the same intensity as $^5L_6\leftarrow{}^7F_0$ transitions; however, their transitions became more intense as compared with other transitions.

Fig. 9(1–4) shows PL emission spectra of $SrWO_4:Eu^{3+}$ powders synthesized by the NHSG method and heat treated at 800 °C for 2, 4, 8 and 16 h when excited at 393 nm ($^5L_6$) at room temperature.

PL emission spectra of $SrWO_4:Eu^{3+}$ powders are dominated by $^5D_{1,0}$ transitions and do not have any ($^5D_2$) transition due to the rapid process of non-radiative relaxation[13]. PL emission spectra show transitions excited state $^5D_{1,0}$ levels to the ground levels; ^7F_J (*J*=0–4) for Eu^{3+} ions for all samples. Multiplets in PL emission spectra are assigned to 2*J*+1 component[9]. The level *J*=0 is non-degenerate, so the $^5D_0\rightarrow{}^7F_0$ transition should show only a band when the Eu^{3+} ion is located in the low symmetry site. Other transitions can have a maximum of three ($^5D_0\rightarrow{}^7F_1$), five ($^5D_0\rightarrow{}^7F_2$), seven ($^5D_0\rightarrow{}^7F_3$) and nine ($^5D_0\rightarrow{}^7F_4$) components if the Eu^{3+} ion is located in sites having only one type of symmetry. $^5D_1\rightarrow{}^7F_J$ (*J*=0–4) transitions occur at about 529.5, 533.6, 551.9, 560.4 and 587.9 nm and are attributed, respectively, to $^5D_1\rightarrow{}^7F_0$, $^5D_1\rightarrow{}^7F_1$, $^5D_1\rightarrow{}^7F_2$, $^5D_1\rightarrow{}^7F_3$ and $^5D_1\rightarrow{}^7F_4$. $^5D_0\rightarrow{}^7F_J$ transitions occur at 578.4, 589.5, 614.4, 649.6 and 700.1 nm, respectively, for $^5D_0\rightarrow{}^7F_0$, $^5D_0\rightarrow{}^7F_1$, $^5D_0\rightarrow{}^7F_2$, $^5D_0\rightarrow{}^7F_3$ and $^5D_0\rightarrow{}^7F_4$ transitions. It is possible to investigate through $^5D_0\rightarrow{}^7F_0$ transitions if the material possesses different luminescent centers; i.e., more than one emissive site. Samples treated at 800 ºC for different treatment time show a peak only at 578.4 nm which indicates one single type of site symmetry for Eu^{3+} ions.

In materials with scheelite-type tetragonal structures (e.g., $SrWO_4$), Sr^{2+} ions are partially replaced by Eu^{3+} ions. Therefore, peak intensities regarding the *f-f* transition at 614.4 nm are related to Eu^{3+} ions located in the A-site without a center of symmetry[60]. $SrWO_4:Eu^{3+}$ powders show a dominant red PL emission (see inset in Fig. 9) which is a characteristic of the electronic transition [$^5D_0\rightarrow{}^7F_2$] at around 614.4 nm. Eu^{3+} ions are an excellent structural probe to investigate the chemical environment. $^5D_0\rightarrow{}^7F_2$ transitions are characteristic of one electric dipole (ED) (hypersensitive) while $^5D_0\rightarrow{}^7F_1$ transitions are related to magnetic dipoles (MD) and are insensitive to change in the local coordination environment in the lattice[2,12,61–63]. The $^5D_0\rightarrow{}^7F_1$ transition is dominant in the inversion symmetry site while in symmetry without an inversion site, the $^5D_0\rightarrow{}^7F_2$ transition

dominates the PL spectra (see Fig. 9(1–4)). These results indicate that Eu^{3+} ions are located in a non-symmetric site such as the scheelite lattice[4,9,12,25]. PL emission spectra have a similarity for all samples which corresponds to typical *f-f* transitions of Eu^{3+} ions. PL emission spectra with excitation at 280 nm (CTB) and 463 nm ($^5D_2$) performed at 77 K and room temperature (not illustrated) have the same profiles but with different absolute intensity. In comparison with the excitation of Eu^{3+} ions, the PL emission intensity of the Eu^{3+} ion is weak under excitation in the CTB which confirms that energy transfer from tetrahedral [WO_4] clusters to Eu^{3+} ions is not efficient.

Using PL emission spectra, it is possible to determine the symmetry site (S_4). To facilitate an understanding of PL emission spectra for $SrWO_4:Eu^{3+}$ powders, the number of bands in each $^5D_1$ and $^5D_0$ transition to ^7F_J is illustrated in Figs. 10(a, b), and their respective positions are listed in Table 7.

It is possible to estimate the expected number of bands in each transition, and therefore [$^5D_1 \rightarrow {}^7F_J$] ($J$=0, 1, 2, 3 and 4) transitions show one peak at 529.5 nm; two peaks at 533.6 and 538.8 nm; four peaks at 551.9, 554.0, 558.3 and 560.4 nm; five peaks at 582.1, 583.9, 584.6, 585.8 and 587.9 nm; and seven peaks at 612.4, 617.6, 618.2, 619.0, 623.3, 625.9 and 627.5 nm, respectively.

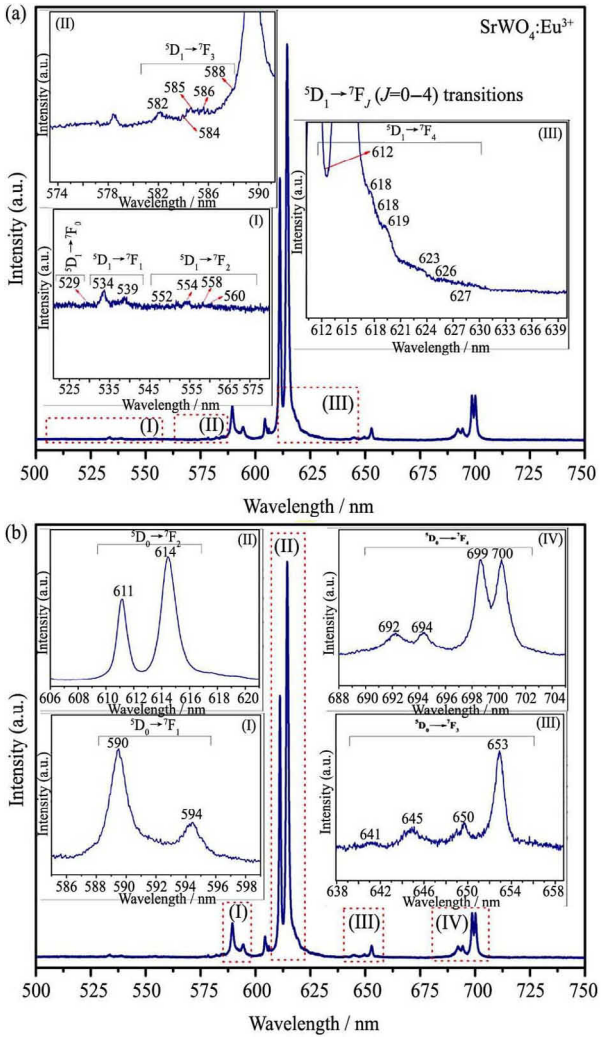

Fig. 10 PL emission spectra of $SrWO_4:Eu^{3+}$ powders heat-treated at 800 ºC for 8 h excited at (λ=393 nm) for bands in each: (a) [$^5D_1 \rightarrow {}^7F_J$] ($J$=0–4) (I, II and III) and (b) [$^5D_0 \rightarrow {}^7F_J$] ($J$=1–4) (I, II, III, and IV) transitions

Table 7 Expected number of band in each transition from the $^5D_{0,1} \rightarrow {}^7F_J$ (J=0–4) to the symmetry site (S_4)

		J=0	J=1	J=2	J=3	J=4
$^5D_0$		0	2	3	4	4
$^5D_1$	$\Gamma_{3,4}$	1	2	4	5	7

According to Bunzli et al.[64], the symmetry site (S_4) peak related to the [$^5D_0 \rightarrow {}^7F_0$] transition should appear, but it is very weak in emission spectra (or does not appear). Therefore, the [$^5D_0 \rightarrow {}^7F_0$] transition can be ascribed to only one weak peak for the PL emission line at 578.4 nm; the $^5D_0 \rightarrow {}^7F_1$ transition has two bands at 589.5 and 594.4 nm, and the $^5D_0 \rightarrow {}^7F_2$ transition has two bands at 611.1 and 614.4 nm. However, the third band is difficult to be observed due to overlapping in the [$^5D_1 \rightarrow {}^7F_4$] transition. The $^5D_0 \rightarrow {}^7F_3$ transition shows four bands at 641.0, 644.9, 649.6 and 652.8 nm. Finally, the $^5D_0 \rightarrow {}^7F_4$ transition has four bands at 692.2, 694.3, 698.6 and 700.1 nm (see Figs. 10(a, b)). The number of bands experimentally observed are in agreement with $^5D_1 \rightarrow {}^7F_J$ and $^5D_0 \rightarrow {}^7F_J$ (J=0–4) transitions as listed in Table 7. Thus, using these results, we conclude that ED and MD transitions for Eu^{3+} ions are strictly obeyed at the S_4 symmetry site[65]. Fig. 4 illustrates that Eu^{3+} ions substitute for Sr^{2+} ions and form deltahedral [EuO_8] clusters located at the A-site.

Fig. 11 displays 3D PL emission spectra of $SrWO_4:Eu^{3+}$ powders heat treated at 800 ºC for different times in the range from 520 to 725 nm as monitored excitations at 393 and 463 nm at room temperature and 77 K.

3D PL emission spectra show the same profile when excited at 393 ($^5L_6$) and 463 nm ($^5D_2$) and performed at 77 K and at room temperature (not illustrated). However,

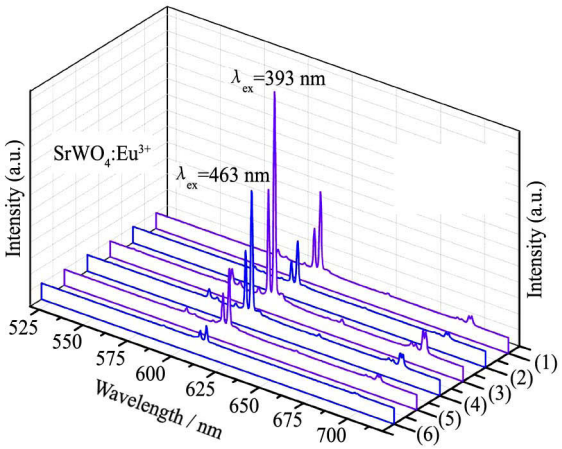

Fig. 11 3D PL emission spectra for $SrWO_4:Eu^{3+}$ powders treated at 800 ºC for: (1, 2) 4 h (3, 4) 8 h and (5, 6) 16 h, λ_{ex}=393 and 463 nm, respectively at 77 K

different intensities are apparent in samples heat treated at different times. Fig. 11 confirms that all transitions are characteristics of Eu^{3+} ions. PL emission spectra displayed in Fig. 11(1), (3) and (5) and excited at 393 nm ($^5L_6$) show that PL emission intensities are dominant as compared with PL emission spectra monitored at 463 nm ($^5D_2$) (see Fig. 11(2), (4) and (6)). Nevertheless, both spectra possess the same profile with the maximum red PL emission at 614.4 nm related to the Eu^{3+} [$^5D_0 \rightarrow {}^7F_2$] transition. PL emission intensity increases significantly as the heat treatment time is raised and attains its maximum value at 800 ºC for 8 h. When the sample was treated above at 800 ºC for 8 h, the PL emission intensity decreased independent of the excitation wavelength used. This phenomenon is known as luminescence quenching which is caused by non-radiative transitions and the energy transfer process. Non-radiative transitions in [$^5L_6 \rightarrow {}^5D_0$] levels and the energy transfer of center activator Eu^{3+} ions to other centers or through lattice defects are believed to be the main processes responsible for luminescence quenching. The similarity between PL emission spectra monitored at 393 and 463 nm indicates that Eu^{3+} ions are located in a single symmetry A-site which indicates that there is one emitter site in these powders.

2.9 Lifetime and quantum efficiency analyses

The decay curves of $SrWO_4:Eu^{3+}$ powders heat treated at 800 ºC for different time related to the $^5D_0 \rightarrow {}^7F_2$ transition of Eu^{3+} ions are shown in Figs. 12(a–d). The excitation and emission wavelength were set at 393 and 614 nm, respectively.

Decay curves for $SrWO_4:Eu^{3+}$ powders related to [$^5D_0 \rightarrow {}^7F_2$] transitions from Eu^{3+} ions and values obtained for optics constants are listed in Table 8. The lifetime (τ), radiative (A_{RAD}) and non-radiative (A_{NRAD}) rates as well as the emission quantum efficiency (η) regarding the $^5D_0$ level were obtained using the equation discussed in previous research[31]. PL emission decay curves of $SrWO_4:Eu^{3+}$ powders show that the fit is related to the mono exponential function (τ=0.60; τ=0.56; τ=0.60, and τ=0.56 ms, respectively); these values are in agreement with PL emission spectra (see Fig. 8).

Table 8 verifies that lifetime values of $SrWO_4:Eu^{3+}$ powders are very close and confirm that all samples exhibit similar structural characteristics which are independent of the variation in heat treatment time. The quantum efficiency for samples heat-treated at 800 ºC for 2, 4, 8, and 16 h showed values of 41.1% (±0.05), 39.7% (±0.05), 40.8%(±0.05) and 34.2%(±0.05), respectively.

A slight decrease in the quantum efficiency is apparent as the heat treatment time increases; unlike behavior was observed for the rate A_{NRAD} (see Table 8). We believe this characteristic may be related to an increase in combinations of non-radiative centers for Eu^{3+} ions which

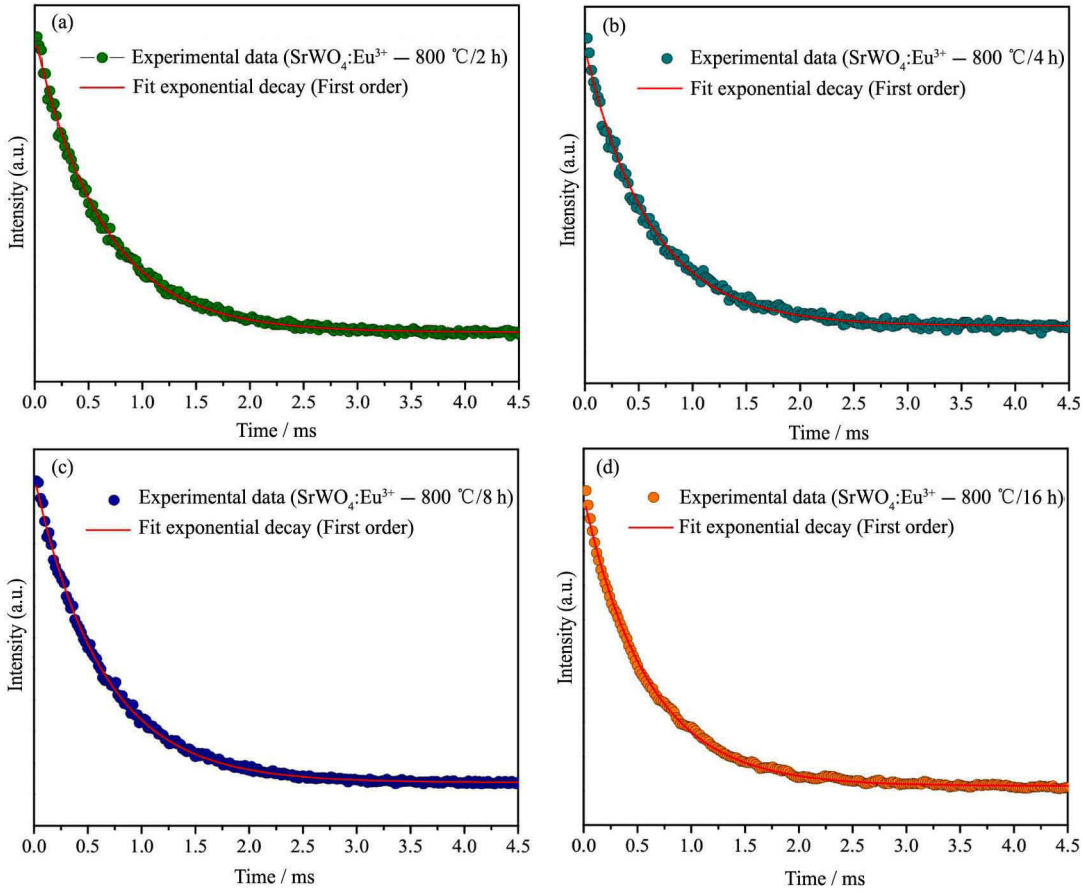

Fig. 12 Decay curves for $SrWO_4:Eu^{3+}$ powders heat-treated at 800 ºC for different times
(a) 2 h; (b) 4 h; (c) 8 h; (d) 16 h

Table 8 Lifetime (τ), radiative (A_{RAD}), non-radiative (A_{NRAD}) rates, emission quantum efficiency (η), relative area of ($I_{0\to2}/I_{0\to1}$) transition and chromaticity (x and y) for the $SrWO_4:Eu^{3+}$ powders heat-treated at 800 ºC for 2, 4, 8 and 16 h

Processing time/h	τ/ms	A_{RAD}/s^{-1}	A_{NRAD}/s^{-1}	η/%	Ω_2/ (10^{-20} cm^2)	Ω_4/ (10^{-20} cm^2)	$I_{0\to2}/I_{0\to1}$	Chromaticity	
								x	y
2	0.60	685	981	41.1 (±0.05)	17.6	4.56	10.0	0.644	0.348
4	0.56	708	1077	39.7 (±0.05)	18.7	4.25	10.6	0.667	0.330
6	0.60	681	986	40.8 (±0.05)	17.3	4.61	9.8	0.657	0.339
8	0.56	611	1175	34.2 (±0.05)	15.0	4.25	8.5	0.623	0.366

contribute strongly to the multiphonon deactivation process at the Eu^{3+} in $^5D_0$ level. The increase in the $A_{N\text{-}RAD}$ rate is probably caused by defects and lattice distortions which promote a recombination of non-radiative centers and decrease the quantum efficiency; consequently, the PL emission intensity decreases. The ratio of the emission intensity for Eu^{3+} $[^5D_0\to{}^7F_2]/[^5D_0\to{}^7F_1]$ transitions provides information about the A-site symmetry where Eu^{3+} ions are located[66]. In addition, this procedure can pinpoint the degree of distortion in the inversion center and the coordination sphere around Eu^{3+} ions in the $SrWO_4$ host matrix[22]. The ratio between the relative area of bands related to $[^5D_0\to{}^7F_2]/[^5D_0\to{}^7F_1]$ transitions in PL emission spectra indicates greater distortion in A-sites due to the low symmetry for Eu^{3+} ions.

Table 8 shows the ratio of $[I_{0\to2}/I_{0\to1}]$ transitions for $SrWO_4:Eu^{3+}$ samples heat treated at 800 ºC for 2, 4, 8 and 16 h. The values do not show large variations, which indicates that Eu^{3+} ions are located at A-sites with low symmetry and occupy network sites without specific inversion symmetry specifically which is consistent with the greater intensity of the $[^5D_0\to{}^7F_2]$ related to $[^5D_0\to{}^7F_1]$ transitions. The intensity of this $[^5D_0\to{}^7F_2]$ transition related to ED is extremely plausible for the ligand environment around Eu^{3+} ions[1,15,61–63].

2.10 International standards chromaticity coordinates (CIE) analyses

The standards chromaticity is considered as a crucial parameter to evaluate the performance of phosphors such as LEDs by analyzing their luminescence efficiency and brightness. CIE patterns available for $SrWO_4:Eu^{3+}$ powders heat treated at 800 ºC for different time of 2, 4, 8 and 16 h are shown in Fig. 13 and are listed in Table 8.

Through CIE analyses, we obtained chromaticity coordinates (x=0.644; y=0.348); (x=0.667; y=0.330); (x=0.657; y=0.339) and (x=0.623; y=0.366) values for $SrWO_4:Eu^{3+}$ powders heat treated at 800 ºC for 2, 4, 8 and 16 h, respectively (see Fig. 13). These values are close to published values for International Standards Chromaticity Coordinates of the commercial phosphor $Y_2O_2S:Eu^{3+}$ (x=0.64; y=0.34)[67]. Fig. 13 shows that color coordinates for our powders are fixed in the red region, which corresponds to the ($^5D_0\to{}^7F_2$) emission of Eu^{3+} ions.

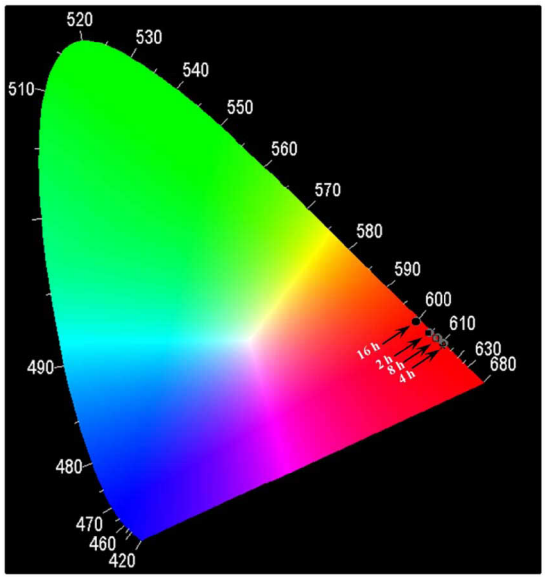

Fig. 13 Chromaticity coordinates of indices to $SrWO_4:Eu^{3+}$ powders obtained by NHSG route synthesized at 800 ºC for: (▪) 2 h, (*) 4 h, (▫) 8 h, and (●) 16 h

3 Conclusions

In summary, the NHSG process is a promising new route to obtain monophasic $SrWO_4:Eu^{3+}$ powders. TG/DTA analyses showed that the crystallization process for the $SrWO_4:Eu^{3+}$ powders occurred at 807 ºC. XRD patterns, Rietveld refinement data and M-Raman spectra showed that $SrWO_4:Eu^{3+}$ powders had a scheelite-type tetragonal structure and were structurally ordered at long and short range. Rietveld refinement data indicated that Eu^{3+} ions were probably located mainly at the A-site; Eu^{3+} ions which caused a slight distortion in the lattice due to their quite different electronic density. UV-vis spectra revealed intermediate energy levels within the "band gap" of this material. PL emission spectra showed all characteristic transitions of Eu^{3+} ions of the excited state to the fundamental $[^5D_{0,1}\to{}^7F_J]$ (J=0–4). The strong PL emission in the red region was related to the electric dipole $[^5D_0\to{}^7F_2]$ transition of Eu^{3+} observed at 614 nm which was caused by the presence of these ions in an environment without an inversion center as confirmed by the $[^5D_0\to{}^7F_0]$ transition. PL properties and ratio values of relative areas for $[^5D_0\to{}^7F_2/{}^5D_0\to{}^7F_1]$ transitions proved that Eu^{3+} ions were located in a low symmetry environment. Through quantum efficiency (η) and life-

time (τ) values, a correlation with the effect of annealing time was confirmed which indicated that the ideal material was obtained after 8 h of heat treatment, since it showed a higher relative intensity when compared to the other samples. The luminescence and CIE data showed that $SrWO_4:Eu^{3+}$ powders had potential for possible applications as red phosphor devices with an excited wavelength of 363 and 462 nm.

Acknowledgments: The authors acknowledge the financial support by the Brazilian research financing institutions: CNPq (No. 142760/2008-0; 479644-2012-8; Postdoctoral No. 160922/2012-7), FAPESP, and CAPES.

References:

[1] Grobelna B. Luminescence based on energy transfer in xerogels doped with $Tb_{2-x}Eu_x(WO_4)_3$. *Opt. Appl.*, 2008, **38**: 39.

[2] Su Y G, Li L P, Li G S. Synthesis and optimum luminescence of $CaWO_4$-based red phosphors with codoping of Eu^{3+} and Na^+. *Chem. Mater.*, 2008, **20**: 6060.

[3] He X H, Guan M Y, Lian N, Sun J H, Shang T M. Synthesis and luminescence characteristics of $K_2Bi(PO_4)(MO_4):Eu^{3+}$(M= Mo, W) red-emitting phosphor for white LEDs. *J. Alloys Compd.*, 2010, **492**: 452.

[4] Shi S K, Liu X R, Gao J, Zhou J. Spectroscopic properties and intense red-light emission of (Ca, Eu, M)WO_4 (M=Mg, Zn, Li). *Spectrochim. Acta Part A*, 2008, **69**: 396.

[5] Guo C F, Chen T, Luan L, Zhang W, Huang D X. Luminescent properties of $R_2(MoO_4)_3:Eu^{3+}$(R=La, Y, Gd) phosphors prepared by sol-gel process. *J. Phys. Chem. Solid.*, 2008, **69**: 1905.

[6] Neeraj S, Kijima N, Cheetham A K. Novel red phosphors for solid-state lighting: the system $NaM(WO_4)_2- x(MoO_4)_x:Eu^{3+}$ (M, Gd, Y, Bi). *Chem. Phys. Lett.*, 2004, **387**: 2.

[7] Qin C X, Huang Y L, Chen G Q, Shi L, Qiao X B, Gan J H, Seo H J. Luminescence properties of a red phosphor europium tungsten oxide Eu_2WO_6. *Mater. Lett.*, 2009, **63**: 1162.

[8] Tian L H, Yang P, Wu H, Li F Y. Luminescence properties of $Y_2WO_6:Eu^{3+}$ incorporated with Mo^{6+} or Bi^{3+} ions as red phosphors for light-emitting diode applications. *J. Lumin.*, 2010, **130**: 717.

[9] Cao F B, Tian Y W, Chen Y J, Xiao L J, Wu Q. Luminescence investigation of red phosphors $Ca_{0.54}Sr_{0.34-1.5x}Eu_{0.08}Sm_x(MoO_4)_y(WO_4)_{1-y}$ for UV-white LED device. *J. Lumin.*, 2009, **129**: 585.

[10] Cao F B, Tian Y W, Chen Y J, Xiao L J, Wu Q. Novel red phosphors for solid-state lighting: $Ca_{0.54}Sr_{0.34-1.5x}Eu_{0.08}La_x(MoO_4)_y(WO_4)_{1-y}$. *J. Alloys Compd.*, 2009, **475**: 387.

[11] Cavalcante L S, Batista F M C, Almeida M A P, Rabelo A C, Nogueira I C, Batista N C, Varela J A, Santos M R M C, Longo E, Siu Li M. Structural refinement, growth process, photoluminescence and photocatalytic properties of $(Ba_{1-x}Pr_{2x/3})WO_4$ crystals synthesized by the coprecipitation method. *RSC. Adv.*, 2012, **2**: 6438.

[12] Lei F, Yan B. Morphology-controlled synthesis, physical characterization, and photoluminescence of novel self-assembled pomponlike white light phosphor: Eu^{3+}-doped sodium gadolinium tungstate. *J. Phys. Chem. C*, 2009, **113**: 1074.

[13] Jia G H, Wang C F, Xu S Q. Local site symmetry determination of scheelite-type structures by Eu^{3+} spectroscopy. *J. Phys. Chem. C*, 2010, **114**: 17905.

[14] Lupei A, Lupei V, Gheorghe C, Gheorghe L, Achim A. Multicenter structure of the optical spectra and the charge-compensation mechanisms in laser crystals. *J. Appl. Phys.*, 2008, **104**: 083102.

[15] Shi S K, Gao J, Zhou J. Effects of charge compensation on the luminescence behavior of Eu^{3+} activated $CaWO_4$ phosphor. *Opt. Mater.*, 2008, **30**: 1616.

[16] Sczancoski J C, Cavalcante L S, Joya M R, Espinosa J W M, Pizani P S, Longo E. Synthesis, growth process and photoluminescence properties of $SrWO_4$ powders. *J. Colloid Interface Sci.*, 2009, **330**: 227.

[17] Maurera M A M A, Souza A G, Soledade L E B, Pontes F M, Longo E, Leite E R, Varela J A. Microstructural and optical characterization of $CaWO_4$ and $SrWO_4$ thin films prepared by a chemical solution method. *Mater. Lett.*, 2004, **58**: 727.

[18] Sczancoski J C, Bomio M D R, Cavalcante L S, Joya M R, Pizani P S, Varela J A, Longo E, Siu Li M, Andrés J A. Morphology and blue photoluminescence emission of $PbMoO_4$ processed in conventional hydrothermal. *J. Phys. Chem. C*, 2009, **113**: 5812.

[19] Jia G, Tu C, You Z, Li J, Zhu Z, Wang Y, Wu B. Czochralski technique growth of pure and rare-earth-doped $SrWO_4$ crystals. *J. Cryst. Growth*, 2004, **273**: 220.

[20] Errandonea D, Pellicer-Porres J, Manjón F J, Segura A, Ferrer-Roca Ch, Kumar R S, Tschauner O, Rodríguez-Hernández P, López-Solano J, Radescu S, Mujica A, Munoz A, Aquilanti G. High-pressure structural study of the scheelite tungstates $CaWO_4$ and $SrWO_4$. *Phys. Rev. B*, 2005, **72**: 174106.

[21] Zhou L Y, Wei J S, Wu J R, Gong F Z, Yi L H, Huang J L. Potential red-emitting phosphor for white LED solid-state lighting. *J. Alloys. Compd.*, 2009, **476**: 390.

[22] Barros B S, De Lima A C, Da Silva Z R, Melo D M A, Alves Jr. S. Synthesis and photoluminescent behavior of Eu^{3+}-doped alkaline-earth tungstates. *J. Phys. Chem. Solid.*, 2012, **73**: 635.

[23] Ju Z H, Wei R P, Gao X P, Liu W S, Pang C R. Red phosphor $SrWO_4:Eu^{3+}$ for potential application in white LED. *Opt. Mater.*, 2011, **33**: 909.

[24] Haque M M, Lee H I, Kim D K. Luminescent properties of Eu^{3+}-activated molybdate-based novel red-emitting phosphors for LEDs. *J. Alloys Compd.*, 2009, **481**: 792.

[25] Liu J, Lian H Z, Shi C S. Improved optical photoluminescence by charge compensation in the phosphor system $CaMoO_4:Eu^{3+}$. *Opt. Mater.*, 2007, **29**: 1591.

[26] Zhao X X, Wang X J, Chen B J, Meng Q Y, Di W H, Ren G Z, Yang Y M. Novel Eu^{3+}-doped red-emitting phosphor $Gd_2Mo_3O_9$ for white-light-emitting-diodes (WLEDs) application. *J. Alloys Compd.*, 2007, **433**: 352.

[27] Liao J S, You H Y, Zhang S A, Jiang J L, Qiu B, Huang H P, Wen H R. Synthesis and luminescence properties of $BaWO_4:Pr^{3+}$ microcrystal. *J. Rare Earths*, 2011, **29**: 623.

[28] Cavalcante L S, Sczancoski J C, Lima L F, Espinosa J W

M, Pizani P S, Varela J A, Longo E. Synthesis, characterization, anisotropic growth and photoluminescence of $BaWO_4$. *Crys. Growth Des.*, 2009, **9**: 1002.

[29] Grobelna B. Luminescence based on energy transfer in xerogels doped with $Ln_{2-x}Tb_x(WO_4)_3$. *J. Alloys Compd.*, 2007, **440**: 265.

[30] Lou Z, Cocivera M. Cathodoluminescence of $CaWO_4$ and $SrWO_4$ thin films prepared by spray pyrolysis. *Mater. Res. Bull.*, 2002, **37**: 1573.

[31] Pereira P F S, De Moura A P, Nogueira I C, Lima M V S, Longo E, De Sousa Filho P C, Serra O A, Nassar E J, Rosa I L V. Study of the annealing temperature effect on the structural and luminescent properties of $SrWO_4$:Eu phosphors prepared by a non-hydrolytic sol-gel process. *J. Alloys Compd*., 2012, **526**: 11.

[32] Hay J N, Raval H M. Synthesis of organic-inorganic hybrids via the non-hydrolytic sol-gel process. *Chem. Mater*., 2001, **13**: 3396.

[33] Hay J N, Porter D, Raval H M. A versatile route to organically-modified silicas and porous silicas via the non-hydrolytic sol-gel process. *J. Mater. Chem*., 2000, **10**: 1811.

[34] Hay J N, Raval H M. Preparation of inorganic oxides via a non-hydrolytic sol-gel route. *J. Sol-Gel Sci. Tech.*, 1998, **13**: 109.

[35] Vioux A. Nonhydrolytic sol-gel routes to oxides. *Chem. Mater.*, 1997, **9**: 2292.

[36] Santos M A, Picon F C, Escote M T, Leite R, Pizani P S, Varela J A, Longo E. Room-temperature photoluminescence in structurally disordered $SrWO_4$. *Appl. Phys. Lett.*, 2006, **88**: 211913.

[37] Cavalcante L S, Sczancoski J C, Albarici V C, Matos J M E, Varela J A, Longo E. Synthesis, characterization, structural refinement and optical absorption behavior of $PbWO_4$ powders. *Mater. Sci. Eng. B*, 2008, **150**: 18.

[38] Nassif V, Carbonio R E, Alonso J A. Neutron diffraction study of the crystal structure of $BaMoO_4$: A suitable precursor for metallic $BaMoO_3$ perovskite. *J. Solid State Chem.*, 1999, **146**: 266.

[39] http://www.crystalimpact.com/diamond/

[40] Bergerhoff G, Berndt M, Brandenburg K. Evaluation of crystallographic data with the program DIAMOND. *J. Res. Natl. Inst. Stand. Techonol*., 1996, **101**: 221.

[41] Cavalcante L S, Sczancoski J C, Tranquilin R L, Joya M R, Pizani P S, Varela J A, Longo E. $BaMoO_4$ powders processed in domestic microwave-hydrothermal: synthesis, characterization and photoluminescence at roomtemperature. *J. Phys. Chem. Solids*, 2008, **69**: 2674.

[42] Ferraro J R, Ziomek J S. Introductory Group Theory and Its Applications to Molecular Structure. 2nd Ed., New York: Plenum Press, 1975.

[43] Nishigaki S, Yano S, Kato H, Nonomura T. $BaO-TiO_2-WO_3$ microwave ceramics and crystalline $BaWO_4$. *J. Am. Ceram. Soc*., 1988, **71**: C11.

[44] Keyson D, Volanti D P, Cavalcante L S, Simões A Z, Souza I A, Vasconcelos J S, Varela J A, Longo E. Domestic microwave oven adapted for fast heat treatment of $Ba_{0.5}Sr_{0.5}(Ti_{0.8}Sn_{0.2})O_3$ powders. *J. Mater. Proc. Tech.*, 2007, **189**: 316.

[45] Basiev T T, Sobol A A, Zverev P G, Ivleva L I, Osiko V V, Powell R C. Raman spectroscopy of crystals for stimulated Raman scattering. *Opt. Mater*., 1999, **11**: 307.

[46] Basiev T T, Sobol A A, Voronko Y K, Zverev P G. Spontaneous Raman spectroscopy of tungstate and molybdate crystals for Raman lasers. *Opt. Mater*., 2000, **15**: 205.

[47] Ling Z C, Xia H R, Ran D G, Liu F Q, Sun S Q, Fan J D, Zhang H J, Wang J Y, Yu L L. Lattice vibration spectra and thermal properties of $SrWO_4$ single crystal. *Chem. Phys. Lett*., 2006, **426**: 85.

[48] Mao Y, Wong S S. General, room-temperature method for the synthesis of isolated as well as arrays of single-crystalline ABO_4-type nanorods. *J. Am. Chem. Soc.*, 2004, **126**: 15245.

[49] Marques A P A, Motta F V, Leite E R, Pizani P S, Varela J A, Longo E, Melo D M A. Evolution of photoluminescence as a function of the structural order or disorder in $CaMoO_4$ nanopowders. *J. App. Phys*., 2008, **104**: 043505.

[50] Nakamoto K. Infrared and Raman Spectra of Inorganic and Coordination Compounds. 4nd Ed.; New York: Wiley, 1996. 477.

[51] Kubelka P, Munk-Aussig F. Ein beitrag zur optik der farban striche. *Zeit. Für. Tech. Physik*., 1931, **12**: 593.

[52] Morales A E, Mora E S, Pal U. Use of diffuse reflectance spectroscopy for optical characterization of un-supported nanostructures. *Rev. Mex. Fis. S*., 2007, **53**: 18.

[53] Smith R A. Semiconductors. 2nd Ed.; London: Cambridge University Press, 1978. 434.

[54] Lacomba-Perales R, Ruiz-Fuertes J, Errandonea D, Martínez-García D, Segura A. Optical absorption of divalent metal tungstates: Correlation between the band-gap energy and the cation ionic radius. *Eur. Phys. Lett*., 2008, **83**: 37002.

[55] Cavalcante L S, Longo V M, Sczancoski J C, Almeida M A P, Batista A A, Varela J A, Orlandi M O, Longo E, Siu L M. Electronic structure, growth mechanism and photoluminescence of $CaWO_4$ crystals. *Cryst. Eng. Commun.*, 2012, **14**: 853.

[56] Longo V M, Orhan E, Cavalcante L S, Porto S L, Espinosa J W M, Varela J A, Longo E. Understanding the origin of photoluminescence in disordered $Ca_{0.60}Sr_{0.40}WO_4$: An experimental and first-principles study. *Chem. Phys.*, 2007, **334**: 180.

[57] Cavalcante L S, Almeida M A P, Avansi W, Tranquilin R L, Longo E, Batista N C, Mastelaro V R, Siu Li M. Cluster coordination and photoluminescence properties of α-Ag_2WO_4 microcrystals. *Inorg. Chem*., 2012, **51**: 10675.

[58] Marques A P A, Longo V M, Melo D M A, Pizani P S, Leite E R, Varela J A, Longo E. Shape controlled synthesis of $CaMoO_4$ thin films and their photoluminescence property. *J. Solid State Chem.*, 2008, **181**: 1249.

[59] Kodaira C A, Brito H F, Felinto M C F C. Luminescence investigation of Eu^{3+} ion in the $RE_2(WO_4)_3$ matrix (RE= La and Gd) produced using the Pechini method. *J. Solid State Chem*., 2003, **171**: 401.

[60] Wang J G, Jing X P, Yan C H, Lin J H, Liao F H. Influence of fluoride on *f–f* transitions of Eu^{3+} in $LiEuM_2O_8$ (M=Mo, W). *J. Lumin.*, 2006, **121**: 57.

[61] Wei Q, Chen D H. Luminescent properties and the morphology of $SrMoO_4:Eu^{3+}$ powders synthesized via combining sol-gel and solid-state route. *Cent. Eur. J. Phys.*, 2010, **8**: 766.

[62] Rosa I L V, Marques A P A, Tanaka M T S, Melo D M A, Leite E R, Longo E, Varela J A. Synthesis, characterization and photophysical properties of Eu^{3+} doped in $BaMoO_4$. *J. Fluoresc.*, 2008, **18**: 239.

[63] Mazzo T M, Moreira M L, Pinatti I M, Picon F C, Leite E R, Rosa I L V, Varela J A, Perazolli L A, Longo E. $CaTiO_3$: Eu^{3+} obtained by microwave assisted hydrothermal method: A photoluminescent approach. *Opt. Mater.*, 2010, **32**: 990.

[64] Bunzli J-C G, Eliseeva S V. Lanthanide Luminescence: Photophysical, Analytical and Biological Aspects, Springer Ser Fluoresc: Basics lanthanide photophysics, Lausanne, Switzerland, 2010.

[65] Binnemans K, Jones P T. Perspectives for the recovery of rare earths from end-of-life fluorescent lamps. *J. Rare Earths*, 2014, **32**: 195.

[66] Zhou L Y, Wei J S, Gong F Z, Huang J L, Yi L H. A potential red phosphor $ZnMoO_4$:Eu^{3+} for light-emitting diode application. *J. Solid State Chem*., 2008, **181**: 1337.

[67] Liao J, You H, Zhou D, Wen H R, Hong R. Sol-gel preparation and photoluminescence properties of $LiLa(MoO_4)_2$: Eu^{3+} phosphors. *Opt. Mater.*, 2012, **34**: 1468.